Growth and characterization of Cu2ZnxFe1-xSnS4 thin films deposited on n-type silicon substrates

M. Sebai, I. Trabelsi, G. Bousselmi, J.-L. Lazzari, M. Kanzari

Growth and characterization of $Cu_2Zn_xFe_{1-x}SnS_4$ thin films deposited on n-type silicon substrates

M. Sebai [a,*], I. Trabelsi [a], G. Bousselmi [a], J.-L. Lazzari [b], M. Kanzari [a,c]

[a] Université de Tunis El Manar, Ecole Nationale d'Ingénieurs de Tunis, Laboratoire de Photovoltaïque et Matériaux Semi-conducteurs, 1002, Tunis, Tunisia
[b] Aix Marseille Univ, CNRS, CINAM, Case 913, Campus de Luminy, Marseille, France
[c] Université de Tunis, ENIT-IPEITunis Montfleury, Laboratoire de Photovoltaïques et Matériaux Semi-conducteurs, Tunisia

ARTICLE INFO

Keywords:
CFTS
CZTS
Solid state reaction
Structural properties
Morphological properties
Electrical properties

ABSTRACT

Cu_2FeSnS_4 and Cu_2ZnSnS_4 ingots were successfully grown by direct melting of their high-purity constituent elements from stoichiometric compositions (copper, iron, zinc, tin and sulfide). Subsequently, thin films of CFTS and CZTS were deposited on unheated n-type silicon substrates through the vacuum evaporation method. These deposited films were sulfided for 30 min at a sulfidation treatment temperature Ts = 400 °C. The structural properties of the C (Z, F)TS thin films were studied by X-ray diffraction (XRD), Raman spectroscopy and electron backscatter diffraction (EBSD).

The resulting studies suggest the existence of polycrystalline phases where CZTS has a kesterite structure and CFTS a stannite structure. Composition analysis also indicates that the synthesized C (Z,F)TS powders are close to the expected stoichiometry.

A good crystallinity of CZTS followed by an increase in the average roughness value of this film is highlighted in the thin film micrographs of C (Z,F)TS. Furthermore, the Hall effect indicates that the prepared C (Z,F)TS films exhibit a manifest p-type semiconductor, and the conductivity, mobility and carrier charge concentration are higher for the CZTS thin film. The electrical conductivity of the CFTS and CZTS thin films were investigated using the impedance spectroscopy technique in the frequency range 5 Hz–13 MH. Values of activation energy are indicative of thermal activation of the conduction mechanism by jumping between localized states. Further, the analysis of the frequency and temperature dependence of the AC conductivity supports the correlated barrier hopping (CBH) model.

1. Introduction

With the increasing demand for traditional energy and the growing issue of global warming, solar cell technology has attracted considerable interest worldwide in terms of research and applications. The Quaternary materials Cu_2ZnSnS_4 (CZTS) and Cu_2FeSnS_4 (CFTS) have been widely explored as suitable absorber layers for solar cell applications. Such materials have the potential as excellent alternatives to Cu(In, GA) Se_2 (CIGS) and CdTe with high efficiency, which involves both rare and toxic elements [1,2]. These two materials belonging to the chalcogenide family offer attractive properties such as high absorption coefficient (>10 4 cm-1), direct band gap (1.54 eV for CZTS and 1.22 eV for CFTS) and occurrence of earth abundant and non-toxic elements [3,4]. Nonetheless, the efficiency of CZTS-based solar cells does not exceed 12.6%, while that of CFTS-based cells remains below 8.3% [5–7]. In order to overcome these limitations, the deposition method and substrate characteristics need to be optimized to design optimal CZTS and CFTS-based thin films.

CZTS and CFTS thin film deposition techniques can be classified into two categories: vacuum-based and non-vacuum-based methods [8]. Vacuum manufacturing processes usually involve the deposition of the basic components of CZTS and CFTS on a substrate by sputtering [9], co-evaporation [10] or evaporation [11] of the target sources under a certain temperature and a certain pressure. Such techniques benefit from the ability to easily control chemical composition and phase and usually present high repeatability [8,12,13].

Vacuum-less deposition techniques include Screen printing [13,14], centrifugal coatings [15,16], sputter pyrolysis [17] and electrochemical deposition [18] of the precursor solutions have been used for the preparation of semiconductor thin films.

* Corresponding author.
E-mail address: Sebai.marwa11@gmail.com (M. Sebai).

https://doi.org/10.1016/j.physb.2023.414670

The present work focuses on the preparation of multicomponent Cu2(Zn, Fe)SnS4 powders, with subsequent analysis of the structural, morphological and electrical properties of Cu2ZnxFe (1-x)SnS4 ingots and thin films (with x = 0, 1) deposited by the single-source vacuum thermal evaporation method on unheated *N*-type silicon substrates, followed by thermal sulfidation under nitrogen flow. It aims to assess the physico-chemical properties of both materials as well as the effect of their deposition on *N*-type silicon substrates, which we present for the first time in this study.

It should be noted that n-type silicon substrates are oriented preferentially (100) and are characterized by a resistance of less than 0.005 Ω and a thickness of between 250 and 700 μm. Such substrates consist of n-type semiconductors into which donor impurities are introduced. Deposition of our materials on these substrates allowed us to generate a *P*–N junction. It is created by combining an n-doped semiconductor (silicon) and a p-doped semiconductor ($Cu_2Zn_xFe_{1-x}SnS_4$). Thin-film photovoltaic technology combined with silicon substrate can offer improved efficiency, along with significant cost-effectiveness, simplicity and ease of manufacturing.

2. Experimental details

The synthesis of CZTS and CFTS ingots was carried out by the direct fusion method. The constituent elements of high purity (99.999%), copper (Cu), zinc (Zn), iron (Fe), tin (Sn) and sulfur (S) were introduced into a quartz tube in conformity with their stoichiometric proportions. The Silica tubes were sealed under a high vacuum of $1{,}33 \times 10^{-6}$ kPa and horizontally placed in a programmable electric furnace (Nabertherm-Germany) following an appropriate profile detailed in the paper [19]. Fig. 1 shows the appearance of the ingots obtained for CFTS and CZTS materials. The CFTS surface exhibits a homogeneous appearance with a gray color while the CZTS ingot presents a blue color. Subsequently, we crushed these ingots to obtain the Cu_2ZnSnS_4 and Cu_2FeSnS_4 powders which will be used as raw materials for the deposition of $Cu_2(Zn,Fe)SnS_4$ thin films (Fig. 2) The deposition was performed with a vacuum thermal evaporator (Alcatel unit) with a molybdenum crucible. Unheated *N*-type silicon wafers were initially used and subsequently sulfided under nitrogen flow at 400 °C for 30 min.

Structural properties of C (Z, F)TS powders and thin films were performed by X-ray diffraction (XRD) with an X'Pert PRO panalytic diffractometer with Bragg-Brentano geometry ($\theta/2\theta$h) using *Cu K* radiation at $k = 1.54056$ Å. To identify the secondary phases of the C (Z, F) TS thin films, Raman spectra were applied. Subsequently, the Electron Backscatter Diffraction (EBSD) technique has been conducted; EBSD was carried out using a scanning electron microscope (SEM) equipped with an EBSD detector with at least one phosphor screen, a low brightness CCD camera and a compact lens. The surface morphology and cross sections of the CZFTS samples were further featured using a scanning electron microscope (Hitachi field effect SEM) coupled to an energy dispersive X-ray spectroscope (EDS) with the accelerating voltage set at 15 kV to check the morphology and thickness of the thin films. In addition, AFM ("atomic force microscopy") analysis of the surface morphology of the thin films was carried out. This AFM technique involved the SPM Multimode (Digital, Santa Barbara, California, USA), equipped with an E-type scanner (scan size: 10 μm × 10 μm, vertical range: 2.5 μm) and a Nanoscope IIIa controller. AFM images were processed in tapping mode using a high-quality probe (HQ-NSC15 from Mikromasch, Sofia, Bulgaria). The electrical properties of the CZTS and CFTS thin films were investigated with a Hall effect analyzer Ecopia AMP55T and an impedance analyzer HP4192A.

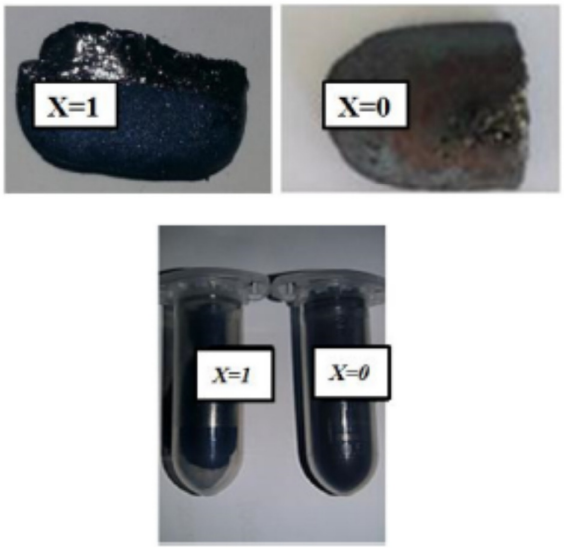

Fig. .1. Ingots and powders of the solid materials $Cu_2(Zn, Fe)SnS_4$.

3. CZTS and CFTS powder

3.1. Structural study

The x-ray diffraction patterns of the Cu_2ZnSnS_4 (CZTS) and Cu_2FeSnS_4 (CFTS) powders in Fig. 2 exhibited distinct diffraction peaks indication that they are both polycrystalline. CZTS (Fig. 3a) displays major peaks situated at 2θ = 23.10°, 28.51°, 29.67°,33.06°, 37.02°, 37.96°, 44.99°, 47.37°, 56.20° and 59.94° which could be referenced to (110), (112), (103), (200), (202), (211), (105), (220)/(204), (312/116) and (224) planes matching the kesterite structure (JCPDS card N° 026–0575 [20]. In addition, an analysis of the XRD diffraction pattern of the synthesized CFTS powder suggests the majority of the peaks relate to the stannite phase of CFTS (JCPDS card N° 00-044-1476) [21]. Those peaks, situated at 2θ = 28.51°,29.85° 33.06°, 36.97°, 37.82°, 40.94°, 45.35°, 47.37°, 56.20° and 59.94° correspond to the (112), (103), (200), (202), (211), (114), (105), (220)/(204), (312)/(116) and (224) planes. Small peaks are seen as well at 2θ = 32.02° and 2θ = 32.97° for CZTS and CFTS respectively, which are consistent with the (004) plane of the SnS phase (JCPDS card 00-053-0526) [22].

It should be mentioned that both materials display a preferred orientation along the diffraction plane (112). It is also possible to detect a shift in this orientation to a small angle of 2θ from CFTS to CZTS clearly. Such variation has been previously reported in other studies [23]. This may be related to the small radius difference between Fe^{2+} (0.66 Å) and Zn^{2+} (0.64 Å) as well as to the transition in phase between the stannite and kesterite phases [24,20].

Based on the XRD analysis, the values of lattice parameters a and c of C (Z, F)TS powders are derived using the formula below for the tetragonal structure:

$$d_{hkl} = \frac{1}{\sqrt{\frac{h^2+k^2}{a^2} + \frac{l^2}{c^2}}} \quad (1)$$

where (*hkl*) are the Miller indices corresponding to XRD peaks and d_{hkl} is the inter-planar spacing given by the Bragg relation

$$2d_{hkl} \sin\theta = n\lambda \quad (2)$$

θ is the Bragg angle and λ is the *Cu-Kα* radiation.

To further explore the structural transition in the C (Z, F)TS semiconductor, we have estimated the tetragonal distortion parameter. Actually, the distortion parameter is an evaluation of the electronic structure of chalcopyrite materials, which is defined by the deviation of the ratio of the long axis 'c' to twice the short axis with respect to $c/2a =$

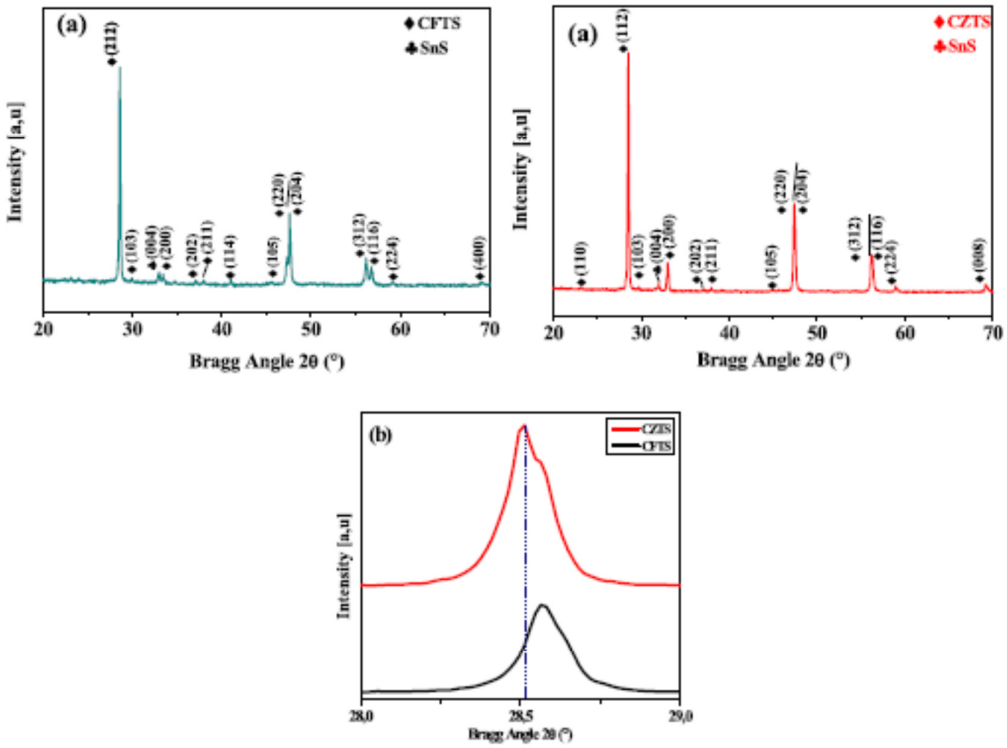

Fig. .2. (a) XRD patterns of synthesized CZTS and CFTS powders, and (b) variation of (112) plane.

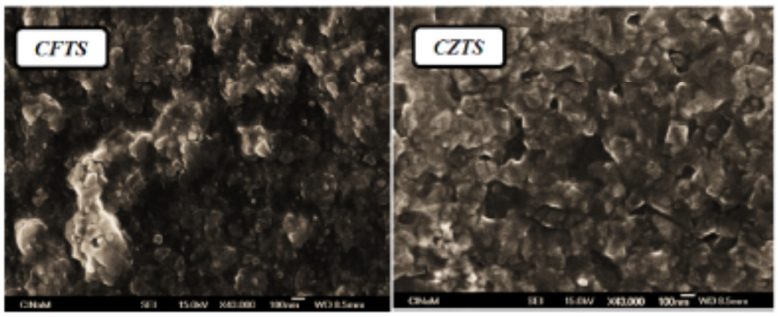

Fig. .3. SEM images of CFTS and CZTS powders.

1 [25]. A summary of values of the lattice parameter, distortion parameter and unit cell volume is provided in Table 1. The calculated lattice parameters for both materials are consistent with those published in previous theoretical and experimental studies [23,24,26,27]. Meanwhile, we notice that the ratio of the distortion coefficient c/2a is close to 1, confirming the tetragonal system [23,28]. The small difference in the distortion parameter might be explained by the difference in the cations in the sublattices in the two structures, kesterite and stannite, crystallizing in two different space groups [23,25,26]. The crystallite size 'D' of the $Cu_2(Zn, Fe)SnS_4$ powders was determined from the predominant peak (112) using Scherer's formula [29]:

$$D = \frac{0.9\lambda}{\beta \cos\theta} \quad (3)$$

where k is the x-ray diffraction wavelength (in *nm*), β is the full width at half maximum (FHWH) (in radians), λ is the x-ray diffraction wavelength (in nm) and θ is the Bragg angle. Table 1 shows the obtained values; we note that the highest crystallite size is obtained for CFTS powder.

Table 1
Lattice **parameters** (a) and (c), distortion parameter and unit cell volume of CFTS and CZTS powders.

	$2\theta_{(112)}$ (°)	a±0.01 (Å)	C± 0.01 (Å)	$\eta = \frac{C}{2a}$ (±0.01)	V± 0.02 (Å^3)	D (nm)
CFTS	28.57	5.43	10.72	0.986	316.08	99
CZTS	28.51	5.42	10.82	0.997	317.84	93

3.2. Composition of CZTS and CFTS powders

Table 2 summarizes the results of the elemental composition of CZTS and CFTS powders performed by the EDS technique. The powders appear homogeneous and close to the expected stoichiometric composition. Nevertheless, the CZTS composition is slightly richer in Cu and Zn and deficient in Sulfur, which might account for the presence of the secondary phase SnS2.

3.3. Morphological study

SEM images of $Cu_2(Zn, Fe)SnS_4$ powders are presented in Fig. 3. It is possible to notice a significant disparity between the surface morphologies of CFTS and CZTS powders. The surface of the CFTS powder contains small and uniformly dispersed grains, and the surface is inhomogeneous and rough. On the other hand, the CZTS powder has a tendency to be compact over the whole surface, indicating the presence of large agglomerations.

4. C (Z, F)TS thin films

4.1. X-ray analysis

The X-ray diffraction technique was implemented to identify the crystallized phases. The XRD patterns of C (Z, F)TS thin films deposited at room temperature on n-type silicon and sulfided under nitrogen flow shown in Fig. 4 exhibit different diffraction peaks indicative of their polycrystallinity For CZTS, various diffraction peaks can be identified that are associated with (110), (112). (200), (103), (200) (004) (211), (220)/(204), (312)/(116) and (224) of the kesterite structure (JCPDS sheet n° 00-026-0575) [30]. In addition, we can identify small amounts of secondary phases that could be associated with the ZnS phase. CFTS thin film reveals distinct diffraction peaks matching with the (200), (004), (204)/(220) and (312)/(116) lattice planes of the stannite structure (JCPDS sheet n° 00- 044–1476) [21]. Similarly, we note the presence of small secondary phases associated with the SnS2, SnS and FeS phases. Moreover, it can be clearly depicted that the dominant peak (112) shifts to lower 2θ angles from CZTS to CFTS. Such a variation, which has been reported by previous studies [24], could be attributed to the transition from stannite (x = 0) to kesterite (x = 1) and small differences in the radius of Fe2+ (0.66 Å) and Zn2+ (0.64 Å) [5,20].

In addition, we can notice a higher intensity for the CZTS thin film towards the preferred orientation plane (112), indicating the good crystal quality of this film. We list all of the microstructural parameters in Table 3. It is important to mention that the crystallite size is higher for the CZTS thin film, which testifies to its good crystallization.

4.2. Raman scattering analysis

Due to the similarity in diffraction peak positions between the quaternary phases CZTS and CFTS and the binary phases ZnS and FeS, Raman spectroscopy provides a valuable identification of the phases present in a material.

Previous research has indicated that the optical modes of the stannite structure (space group I-42m) can be described by the following formula: = A1 + A2 + 2B1 + 4B2 + 6 E, where A1 is given to the symmetry mode that corresponds to the strongest line of the Raman spectra. For more details, B2 and E modes are active IR modes that exhibit LO-TO splitting due to their polar characteristics, while A2 mode is not an active Raman mode. The structure of kesterite (space group I4) indicates the optical modes as follows: Γ = 3 A + 6 B + 6 E. Fig. 5 shows the Raman spectrum of CFTS and CZTS thin films recorded at room temperature.

For the CZTS thin film, we note that the majority of the peaks are attributed to the CZTS phase with in particular very strong peaks at 332 cm^{-1} which correspond perfectly to the A mode of the CZTS kesterite phase as reported in the literature [31]. We also notice that CZTS presents a significant peak at 285 cm^{-1} corresponding to the (A) mode as

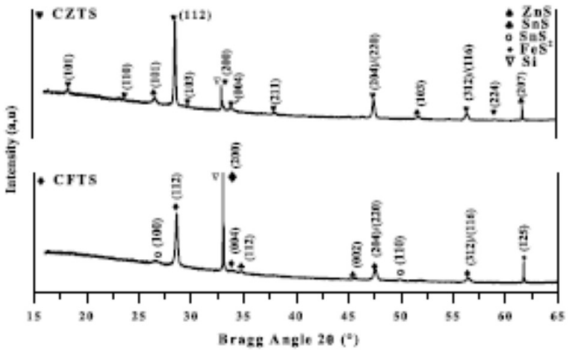

Fig. .4. XRD patterns of $Cu_2(Zn, Fe)SnS_4$ thin films.

Table 3
Microstructural parameters of CFTS and CZTS thin films.

	2θ(°)	β(°)	D (nm)
CFTS	28.57	0.22	72
CZTS	28.59	0.16	99

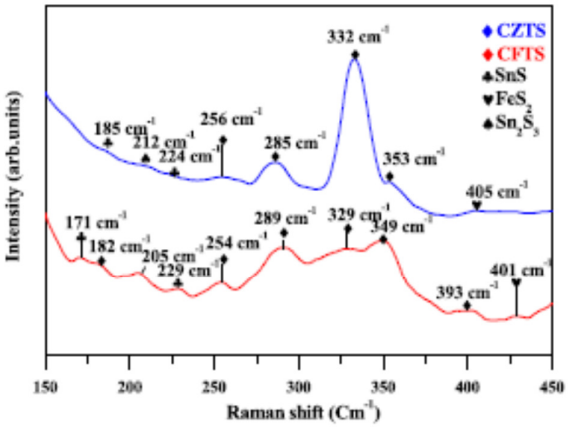

Fig. .5. Raman spectra of CFTS and CZTS thin films.

Table 2
Elemental compositions of CFTS and CZTS powders.

Theoretical compositions	Elements in atomic percentage (%)					Experimental Compositions
$Cu_2Zn_xFe_{1-x}SnS_4$	Cu (±2)	Fe (±3)	Zn (±3)	Sn (±2)	S (±3)	$Cu_2Zn_xFe_{1-x}SnS_4$
Cu_2FeSnS_4	25.54	12.99	0	12.10	49.01	$Cu_{2.04}Fe_{1.03}Sn_{0.96}S_{3.92}$
Cu_2ZnSnS_4	29.04	0	13.77	11.73	45.43	$Cu_{2.32}Zn_{1.10}Sn_{0.93}S_{3.63}$

well as other minor peaks at 256 cm^{-1} and 353 cm^{-1} which could be attributed to the B2 modes [31–35]. As a result, we note the presence of low intensity impurity phases corresponding to SnS (186 cm^{-1}, 224 cm^{-1}), Sn_2S_3 (212 cm^{-1}) and FeS_2 (405 cm^{-1}) binaries [36–38]. The CFTS thin films also display two dominant Raman peaks located at 289 cm^{-1} and 349 cm^{-1} ascribed to the A1 and E modes of the stannite structure.

Furthermore, we could notice other minor peaks at 182 cm^{-1}, 254 cm^{-1}, 329 cm^{-1}, and 393 cm-1 attributed to B2 and A1 modes, which are consistent with the literature [31,33,39]. As well, it is possible to identify weak peaks with low intensity that could be attributed to binary secondary phases SnS (171 cm^{-1} and 229 cm^{-1}) and FeS2 (401 cm^{-1}) [31,33,38,39]. Previous work [26] suggests that this shift may be related to the vibration of the pure sulfur anion, since the A1 and A symmetry modes also depend on the Fe–S and Zn–S bond. From these expected results, it appears that the Raman measurements are consistent with the XRD analysis as well as the presence of CZTS and CFTS phases. It is possible to confirm that the best homogeneity and crystallinity is obtained for the CZTS thin film.

4.3. Electron BackScatter diffraction (EBSD)

The structural analysis was carried out by EBSD. Indeed, through this technique, it is possible to identify the phases of the material and to assign orientation planes. The ICDD database was also used as a reference. Although this method is more focused than the XRD technique, multiple points were analysed in each sample. To perform an EBSD measurement, a flat, polished polycrystalline sample is placed in the SEM chamber at a steep angle (−70° from horizontal) toward the diffraction camera to increase the contrast of the backscattered electron pattern [40].

Fig. 6 shows the electron diffraction pattern for the CZTS and CFTS thin films. From this plate, we can clearly distinguish the presence of (1−11) plane for both materials, according to the ICDD database, these results reflect the highest percentage [100%] of tetragonal kesterite structure CZTS (I-4) and stannite (I4-2m). This supports the findings of the XRD technique, namely the identification of the tetragonal CZTS and CFTS, Our study was able to recognize only the main phase of the materials as a result of their high roughness.

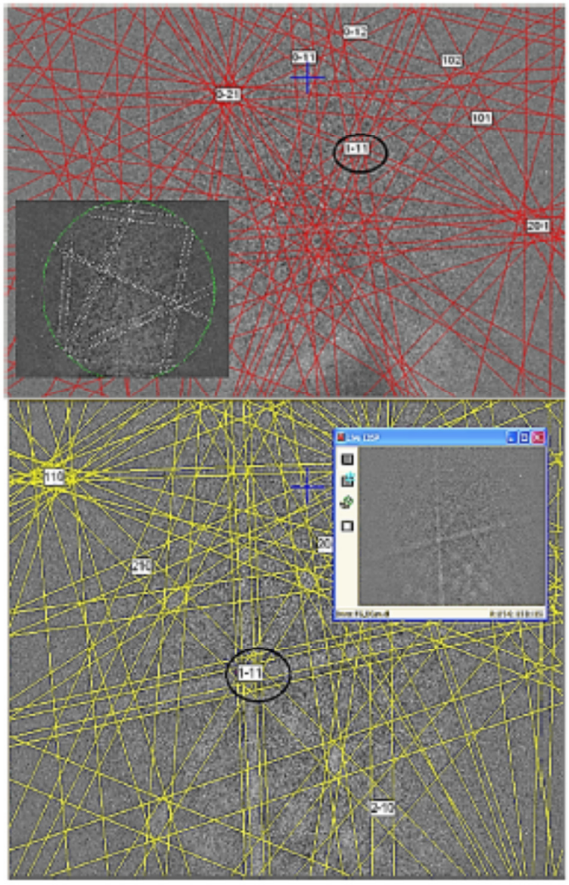

Fig. .6. Electron diffraction pattern for the CZTS and CFTS thin films.

4.4. Chemical compositions of CZTS and CFTS thin films

EDS measurements were performed to evaluate the stoichiometry of CZTS and CFTS thin films deposited at room temperature on *n-type* silicon substrates. This study revealed the presence of the constituent elements of each material (Cu, Zn, Fe, Sn and S) in the CZTS and CFTS materials. The proportions for each element are presented in Fig. 7. In addition, the atomic percentages obtained from EDS measurements are provided for all the different films processed in Table 4.

We revealed that the obtained compositions of the CZTS thin film are very close to the expected stoichiometry with a small deficiency in copper and sulfur. The proportions are close to unity, which justifies the good crystallinity of the CZTS material. On the other hand, a composition far from the desired stoichiometry was obtained for the CFTS thin film. This thin film presents an excess of copper, iron and tin and a deficit of sulfur, leading to the formation of binary SnS, SnS_2 and FeS secondary phases of low intensity, the calculated ratios are also far from unity, which can affect the crystallinity of the thin layer.

4.5. Morphological study

In order to describe the surface morphology of $Cu_2(Zn, Fe)SnS_4$ thin films, scanning electron microscopy was performed. Fig. 8(a), (b) and (d) displays the cross-sectional area and surface morphology of CZTS and CFTS films, respectively. A significant difference between the structure of CZTS and CFTS is evident from these figures. The micrograph of the CFTS film (Fig. 8a) shows small grains confirming the low crystallinity observed in the XRD results, the character of the film is uniformly compact with no overgrain formation. However, we also note the presence of voids between the grains, reducing the transition of electrons between the grains and thus affecting the conductivity of the thin film.

The surface of CZTS has good crystalline textures with well-developed grains, making it suitable for photovoltaic application. We note, then, that the surface is porous and inhomogeneous. In lower magnification surface measurements (Fig. 8b), a dendritic growth was observed for CZTS thin films, which might be accounted for by the presence of a heterojunction between the material (*p-type*) [41] and the substrate (*n-type*). To further validate this aspect, an optical microscope was used (Fig. 8c), the resulting images confirm the dendritic morphology for the CZTS thin films and the composition of the CFTS surface into small grains separated by voids. The cross-sectional images (Fig. 8d) reflect complete crystallization with a very compact nature for the CZTS thin films with larger grain sizes emerging. Additionally, it was possible to estimate the thickness of these thin films from these images. We found that the thickness of CFTS is approximately 350 ± 20 nm while that of CZTS is about 400 ± 20 nm, consistent with previous results [19]. From the AFM measurement (Fig. 9), the average roughness of 15.21 nm for the CFTS thin film and 66.10 nm for the CZTS may reflect the improved crystallinity of the films as mentioned. This is consistent with the increase in thickness of these thin films. Additionally, the micrographs taken reveal a surface composed of small grains

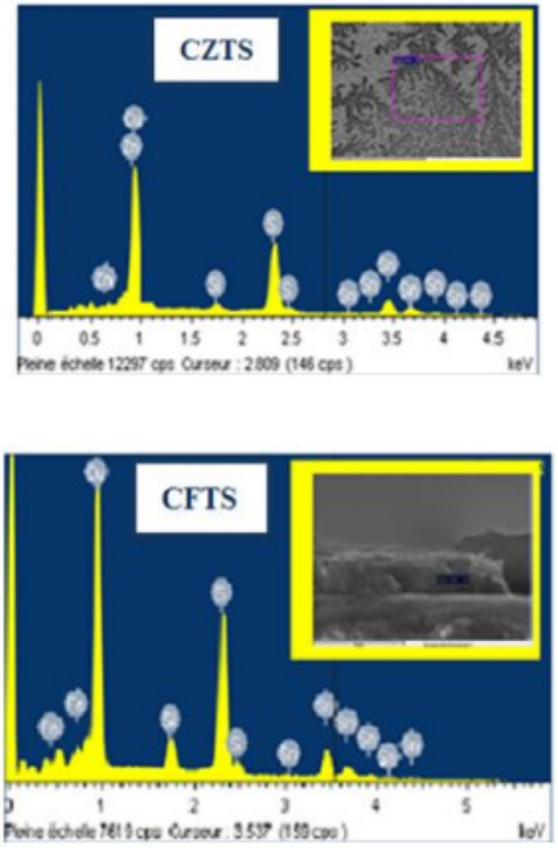

Fig. .7. Chemical composition of the C (Z, F)TS.

separated by void for CFTS and large agglomerated grains for CZTS, coherent with the resulting SEM images.

4.6. Electrical properties

4.6.1. Hall effect

An investigation of the electrical properties of $Cu_2(Zn, Fe)GnS_4$ thin films was carried out by measuring the Hall effect at room temperature. The films have a *p-type* conductivity [41]. The carrier concentration, conductivity, resistivity and mobility of the films are provided in Table 5. We note that the carrier concentration, conductivity and Hall mobility increases from CFTS to CZTS. This increased mobility could be attributed to the enhanced crystallinities and grain sizes [42], as shown by XRD, Raman, FE-SEM and AFM analyses. Similarly, it is noted that the increase in crystallite size of the CZTS thin film leads to a reduction in inter-crystalline scattering and an increase in carrier durability, which increases mobility [43,44].

The presence of secondary phases has been reported to affect the electrical properties of thin films [45]. So, the minor peaks attributed to the SnS_x secondary phase formed for the CFTS thin film affect its electrical properties. Since mobility is inversely proportional to resistivity, the removal of the SnS secondary phase increases the mobility of the thin film, which further reduces the resistivity and thus improves the overall electrical properties of the thin film. We also notice that the secondary phases are a minority for CZTS which account for the large values found for the carrier concentration, mobility and conductivity.

4.6.2. Impedance spectroscopy

The process of impedance spectroscopy is an effective technique that allows identifying the contributions of various processes such as electrode effects, grain effects, interfaces in thin films and dielectric properties [46,47].

Fig. 10 depicts the complex impedance spectra ($-Z''$ versus Z') derived by plotting the imaginary part with the respective real part for CFTS and CZTS thin films [41]. The CFTS thin film Nyquist plot displays a large capacitive loop in the high frequency region and an inductive loop in the low frequency region. Note that the inductive loop tends to close in on itself, giving rise to another capacitive loop indicating the active transition of the semiconductor. However, in (A) of Fig. 10, RL in series with L is connected in parallel with the circuit (R_bC_b), where R_b and C_b are the resistance and capacitance of the grain, respectively, RL and L denote the constant phase element (CPE), resistance and inductance, respectively [48]. Furthermore, the impedance diagrams reveal that the semicircles show a slight depression and their maximum shifts to higher frequencies with increasing temperature. The diameter and maximum of the semicircles for CFTS also decrease with increasing temperature. These observations lead to the conclusion that the electrical conductivity is thermally activated as well as the relaxation time distribution [49].

For CZTS thin films, a semicircular arc is highlighted in the impedance diagram, indicating R_bC_b elements parallel to the grains. It is convenient to indicate that each semicircle was an equivalent circuit treated as a combination of resistor and capacitor usually placed in parallel, as shown in Fig. 10 (B). The resulting semicircles are slightly depressed and their centers are shifted downward from the actual axis, showing the unique relaxation process. A depressed arc is also typical of a dipolar system involving multiple relaxation processes [46,50–52]. Similarly, the semicircles could indicate the homogeneity of evaporated CZTS thin films, which is in good agreement with the morphological and structural results.

Accordingly, to explore the relaxation time as a function of temperature, we plotted $-Z''$ versus frequency at different temperatures (Fig. 11). We found that the $-Z''$ exhibits a maximum ω_m (ω_m defined as

Table 4
Composition results of CFTS and CZTS films obtained by EDX technique.

Elements (Atomic %)	Theoretical results		Experimental results	
	Cu_2FeSnS_4	Cu_2ZnSnS_4	$Cu_{2.34}Fe_{1.42}Sn_{1.17}S_{3.31}$	$Cu_{1.86}Zn_{1.13}Sn_{1.03}S_{3.96}$
Cu	25	25	28.07	23.30
Zn	0	12.5	0	14.21
Fe	12.5	0	15.76	0
Sn	12.5	12.5	14.73	12.89
S	50	50	41.44	49.60
Zn/Sn	0	1	0	1.10
Fe/Sn	1	0	1.06	0
S/Metal	1	1	0.70	0.98
Cu/(Zn + Sn)	0	1	0	0.85
Cu/(Fe + Sn)	1	0	0.92	0

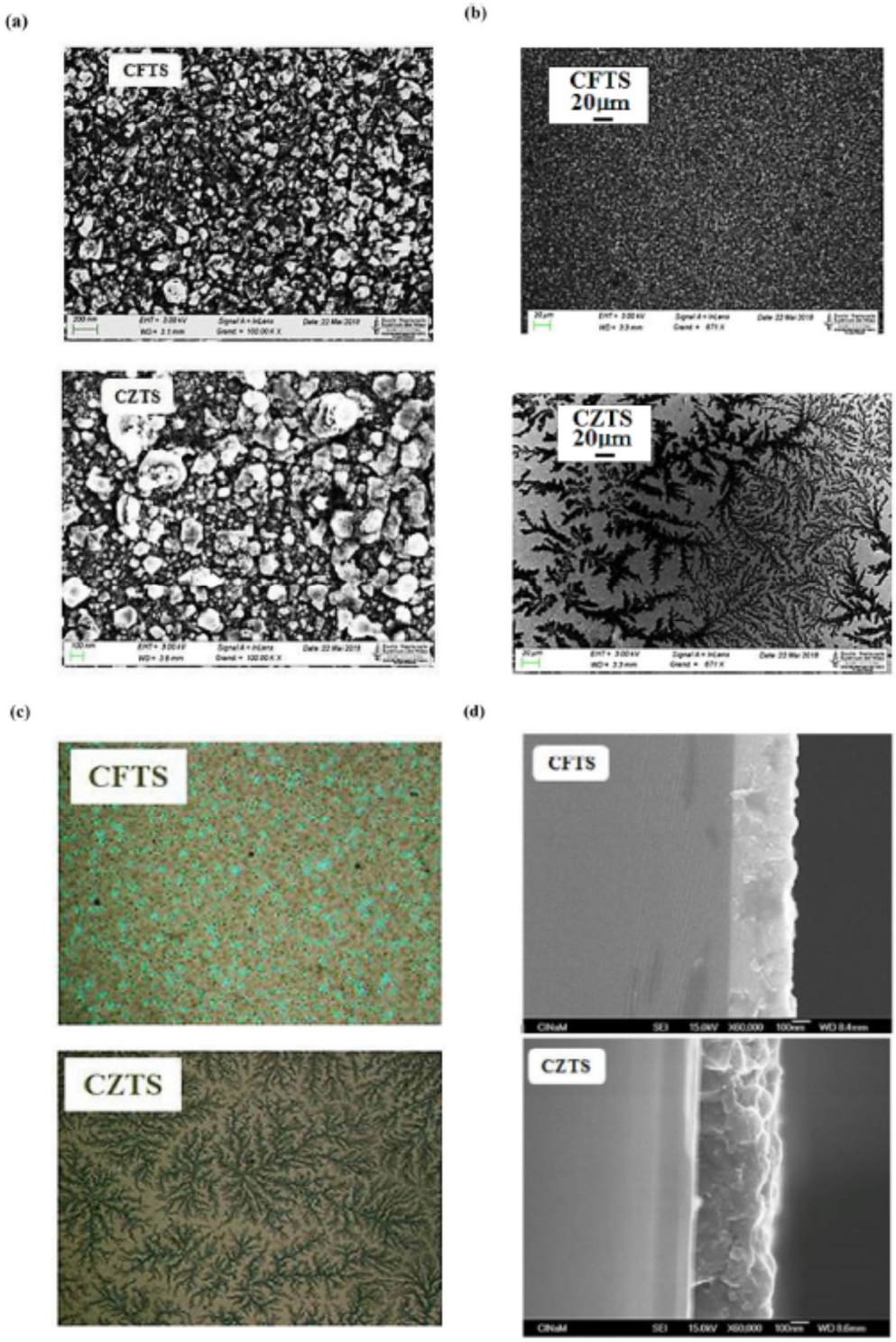

Fig. .8. (a) and (b) Plane-view field-emission scanning electron microscopy (FE–SEM) images of CXTS thin films deposited with x — Fe and Zn respectively, (c) images of CFTS and CZTS respectively performed by scanning optical microscope, (d) cross-section image for C (Z, F)TS thin films.

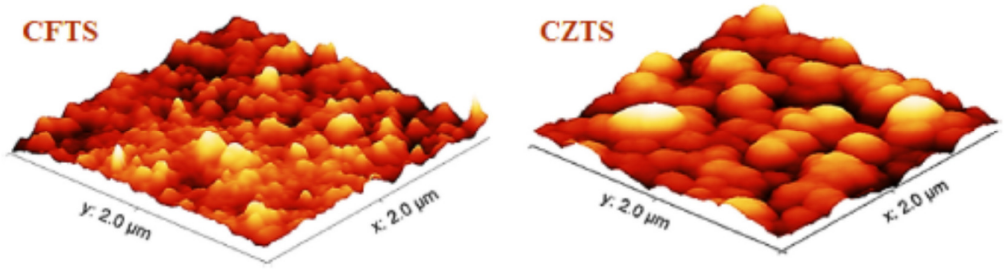

Fig. .9. 3D AFM images respectively of CFTS and CZTS thin films.

Table 5
Hall Effect measurement results of CFTS and CZTS thin films.

Substrate type	Carrier concentration (cm^{-2})	Conductivity ($\Omega.cm)^{-1}$	Resistivity ($\Omega.cm$)	Mobility (cm^2/Vs)
CFTS	1.83×10^{19}	272	3.6×10^{-3}	312
CZTS	2.12×10^{21}	483	2.07×10^{-3}	295

$\omega_m \times \tau = 1$) that shifted to a higher frequency by increasing the temperature [53]. Moreover, we could find that the frequency of the peak indicates an Arrhenius behavior and we can then estimate the activation energy. The relaxation time of these samples obeys the famous Arrhenius law [54]:

$$\omega_m = \omega_0 e^{\frac{-E_a}{K_B T}} \quad (4)$$

ω_0 is a constant, k_B is the Boltzmann constant, and Ea is the activation energy. A summary of the Ea values for CFTS and CZTS is presented in Table 6. As shown in Fig. 11, the spectra for Ln (ω_m) = f (1/T) exhibit a linear feature, in good agreement with the expression (4).

To further assess the DC transmission characteristics results, we investigated the AC response of CFTS and CZTS thin films to identify and differentiate the origin of the conduction process. The electrical conductivity can be calculated using the relation [50]:

$$\sigma_{AC} = \sigma_{DC} + A\omega^s \quad (5)$$

The variation of electrical conductivity at different temperatures as a

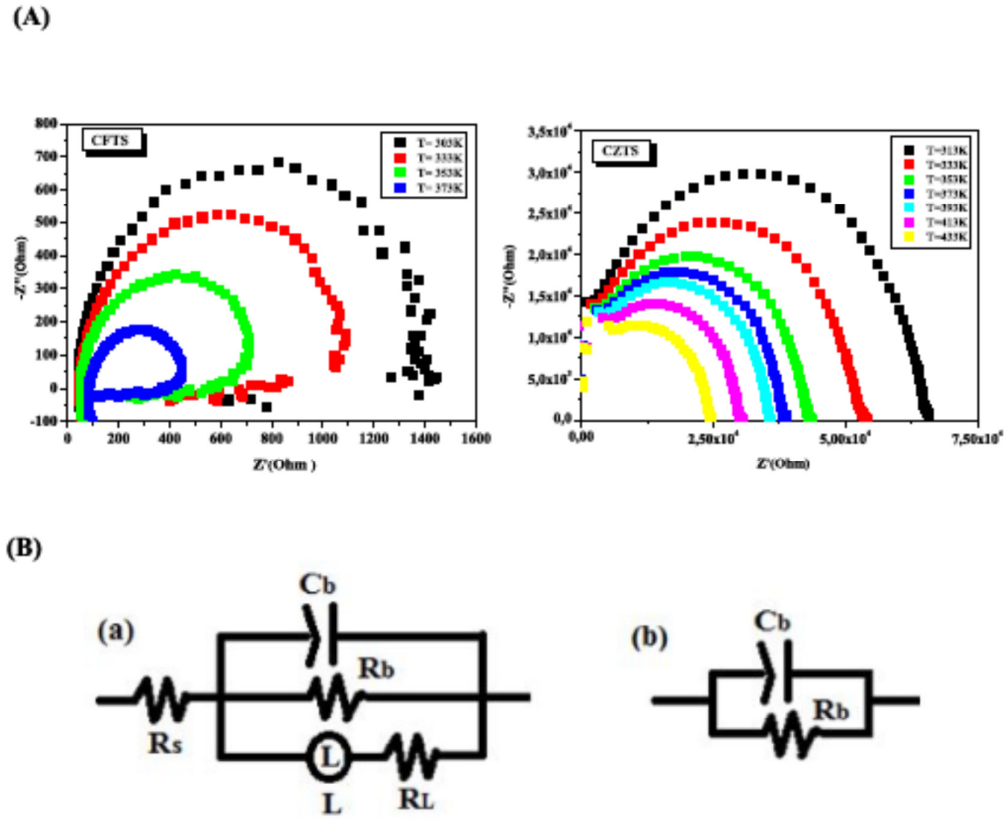

Fig. .10. Nyquist diagram of CFTS and CZTS thin films and the equivalent circuits (B) of CFTS (a) and CZTS (b).

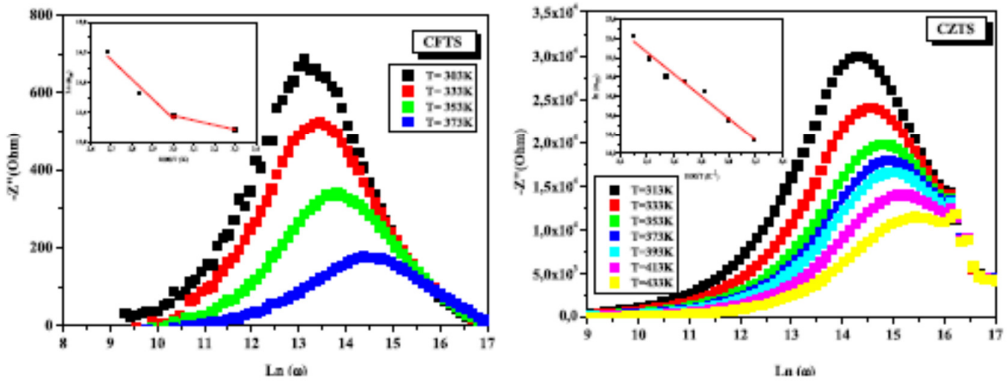

Fig. .11. Angular frequency dependence of Z'' at different temperatures for CFTS and CZTS thin films.

Table 6
Calculated values of E_a for CFTS and CZTS.

	CFTS		CZTS
Ea (eV)	$Ea_1 = 3.24$	$Ea_2 = 0.77$	1.14

function of frequency is depicted in Fig. 12.

A stable conductivity is found for impulsions below ω_H, that could be assigned to the formation of free charges in the films [51]. It is also possible to detect a shift of the AC conductivity to a higher frequency with temperature, which is consistent with a thermally activated process [55,56]. The frequency dependence of the conductivity is indicative of jump conduction at a higher frequency between localized states [57,58].

In general, the variation of ''s'' with temperature is associated with the conduction mechanism and can be derived from the slopes of the ln (σ_{AC}) versus ln(ω) curves at different temperatures [52]. This parameter ''s'' is generally employed to further characterize the interaction between the different charge species involved in the polarization process as well as to describe the AC component contributing to the dispersive region [51,52] (Fig. 12).

These values are below unity, suggesting the presence of extrinsic dipoles or charge carriers resulting from impurities and defects in the film [59,60]. Additionally, it decreases with increasing temperature which could be in accordance with the Correlated Barrier Hopping (CBH) model presented by Elliot et al. [61,62]. This model suggests that the hopping of charge carriers between sites on the potential barrier between them attenuates with increasing temperature [66, 67].

5. Conclusion

In this paper, Cu_2FeSnS_4 and Cu_2ZnSnS_4 powders were synthesized by the direct fusion method. The X-ray diffraction analysis of these powders reveals that the CFTS powder crystallizes in the stannite structure, while the CZTS powder crystallizes in the kesterite structure. Crushed powder was employed as a source for the fabrication of CFTS and CZTS thin films by thermal vacuum evaporation method followed by sulfidation. A study of the structural, morphological and electrical properties of these thin films was carried out. The obtained results showed that only $Cu_2ZnFeSnS_4$ exhibits good crystallinity, improved surface morphology and excellent electrical properties. Such properties make this material a suitable candidate to be used as absorber material in solar cells.

Author contribution

Marwa Sebai: Visualization, Writing. Imen Trabelsi: Formal analysis. Ghada Bousselmi: Review & Editing. Jean-Louis Lazzari: Validation. Mounir Kanzari: Supervision.

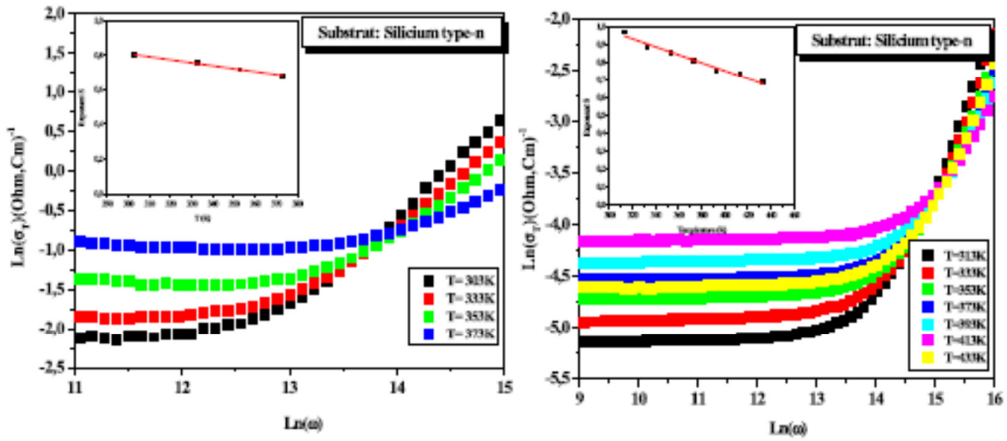

Fig. .12. Angular frequency dependence of AC conductivity at different temperature for $Cu_2(Zn, Fe)SnS_4$ thin films.

Compliance with Ethical Standards

☒ This material is the authors' own original work, which has not been previously published elsewhere.
☒ The authors declare that this article does not contain any studies involving human participants performed by any of the authors.
☒ The results are appropriately placed in the context of prior and existing research.

Declaration of competing interest

The authors declare that they have no known competing financial interests or personal relationships that could have appeared to influence the work reported in this paper.

Data availability

No data was used for the research described in the article.

References

[1] M.A. Green, K. Emery, Y. Hishikawa, W. Warta, E.D. Dunlop, Solar cell efficiency tables (version 42), Prog. Photovoltaics Res. Appl. 21 (2013) 827–837, https://doi.org/10.1002/pip.2404.

[2] C. Wadia, A.P. Alivisatos, D.M. Kammen, Materials availability expands the opportunity for large-scale photovoltaics deployment, Environ. Sci. Technol. 43 (2009) 2072–2077, https://doi.org/10.1021/es8019534.

[3] W. Wang, M.T. Winkler, O. Gunawan, T. Gokmen, T.K. Todorov, Y. Zhu, D.B. Mitzi, Device characteristics of CZTSSe thin-film solar cells with 12.6% efficiency, Adv. Energy Mater. 4 (2014), 1301465, https://doi.org/10.1002/aenm.201301465.

[4] R.R. Prabhakar, N. Huu Loc, M.H. Kumar, P.P. Boix, S. Juan, R.A. John, S. K. Batabyal, L.H. Wong, Facile water-based spray pyrolysis of earth-abundant Cu 2 FeSnS 4 thin films as an efficient counter electrode in dye-sensitized solar cells, ACS Appl. Mater. Interfaces 6 (2014) 17661–17667, https://doi.org/10.1021/am503888v.

[5] M. Quintero, E. Moreno, S. Alvarez, J. Marquina, C. Rincón, E. Quintero, P. Grima, J.-A. Heano, M.A. Macías, LATTICE PARAMETER VALUES AND PHASE TRANSITIONS FOR THE Cu2-II-IV-S4(Se4) (II=Mn, Fe, Co; IV=Si, Ge, Sn) MAGNETIC SEMICONDUCTOR COMPOUNDS, Rev. Lat. Met. Mat. 1 (2014) 28–38.

[6] O.V. Parasyuk, L.V. Piskach, Y.E. Romanyuk, I.D. Olekseyuk, V.I. Zaremba, V. I. Pekhnyo, Phase relations in the quasi-binary Cu2GeS3–ZnS and quasi-ternary Cu2S–Zn(Cd)S–GeS2 systems and crystal structure of Cu2ZnGeS4, J. Alloys Compd. 397 (2005) 85–94, https://doi.org/10.1016/j.jallcom.2004.12.045.

[7] H. Matsushita, A. Katsui, Materials design for Cu-based quaternary compounds derived from chalcopyrite-rule, J. Phys. Chem. Solid. 66 (2005) 1933–1936, https://doi.org/10.1016/j.jpcs.2005.09.028.

[8] H. Wang, Int. J. Photoenergy (2011), https://doi.org/10.1155/2011/801292, 1–10.

[9] R. Touati, M. Ben Rabeh, M. Kanzari, Structural and optical properties of the new absorber Cu 2ZnSnS4 thin films grown by vacuum evaporation method, Energy Proc. 44 (2014) 44–51, https://doi.org/10.1016/j.egypro.2013.12.008.

[10] T. Tanaka, D. Kawasaki, M. Nishio, Q. Guo, H. Ogawa, Fabrication of Cu 2 ZnSnS 4 thin films by co-evaporation, Phys. Status Solidi C 3 (2006) 2844–2847, https://doi.org/10.1002/pssc.200669631.

[11] R. Kaur, S. Kumar, S. Singh, Vapour Phase Techniques for Deposition of CZTS Thin Films: A Review, 2018, 100039, https://doi.org/10.1063/1.5032975.

[12] K. Woo, Y. Kim, J. Moon, A non-toxic, solution-processed, earth abundant absorbing layer for thin-film solar cells, Energy Environ. Sci. 5 (2012) 5340–5345, https://doi.org/10.1039/C1EE02314D.

[13] Q.M. Chen, X.M. Dou, Z.Q. Li, S.Y. Cheng, S.L. Zhuang, Preparation of film by printing process for low-cost solar cell, Adv. Mater. Res. 335–336 (2011) 1406–1411. https://dx.doi.org/10.4028/www.scientific.net/AMR.335-336.1406.

[14] Z. Zhou, Y. Wang, D. Xu, Y. Zhang, Fabrication of Cu2ZnSnS4 screen printed layers for solar cells, Sol. Energy Mater. Sol. Cells 94 (2010) 2042, https://doi.org/10.1016/j.solmat.2010.06.010. –2045.

[15] T.K. Todorov, K.B. Reuter, D.B. Mitzi, High-efficiency solar cell with earth-abundant liquid-processed absorber, Adv. Mater. 22 (2010), https://doi.org/10.1002/adma.200904155, 156–159.

[16] K. Tanaka, M. Oonuki, N. Moritake, H. Uchiki, Cu2ZnSnS4Cu2ZnSnS4 thin film solar cells prepared by non-vacuum processing, Sol. Energy Mater. Sol. Cells 93 (2009) 583–587, https://doi.org/10.1016/j.solmat.2008.12.009.

[17] V.G. Rajeshmon, C.S. Kartha, K.P. Vijayakumar, C. Sanjeeviraja, T. Abe, Y. Kashiwaba, Role of precursor solution in controlling the opto-electronic properties of spray pyrolysed Cu2ZnSnS4 thin films, Sol. Energy 85 (2011) 249–255, https://doi.org/10.1016/j.solener.2010.12.005.

[18] C.P. Chan, H. Lam, C. Surya, Preparation of Cu2ZnSnS4 films by electrodeposition using ionic liquids, Sol. Energy Mater. Sol. Cells 94 (2010) 207–211, https://doi.org/10.1016/j.solmat.2009.09.003, https://doi.org/10.1016/j.solmat.2009.09.003.2010) 207–211.

[19] A. Hannachi, H. Oueslati, N. Khemiri, M. Kanzari, Effects of sulfurization on the optical properties of Cu2ZnxFe1-xSnS4 thin films, Opt. Mater. 72 (2017) 702–709, https://doi.org/10.1016/j.optmat.2017.07.031.

[20] C. Huang, Y. Chan, F. Liu, D. Tang, J. Yang, Y. Lai, J. Li, Y. Liu, Synthesis and characterization of multicomponent Cu2(FexZn1 –x)SnS4 nanocrystals with tunable band gap and structure, J. Mater. Chem. A. 1 (2013) 5402, https://doi.org/10.1039/c3ta00191a.

[21] JCPDS card number 00-044-1476.

[22] JCPDS card number 00-053-0526.

[23] D.B. Khadka, J. Kim, Structural transition and band gap tuning of Cu 2 (Zn,Fe)SnS 4 chalcogenide for photovoltaic application, J. Phys. Chem. C 118 (2014) 14227–14237, https://doi.org/10.1021/jp503678h.

[24] Z. Shadrokh, A. Yazdani, H. Eshghi, Solvothermal synthesis of Cu 2 Zn 1– x Fe x SnS 4 nanoparticles and the influence of annealing conditions on drop-casted thin films, Semicond. Sci. Technol. 31 (2016), 045004, https://doi.org/10.1088/0268-1242/31/4/045004.

[25] S. Siebentritt, S. Schorr, Kesterites-a challenging material for solar cells, Prog. Photovoltaics Res. Appl. 20 (2012) 512–519, https://doi.org/10.1002/pip.2156.

[26] P. Bonazzi, L. Bindi, G.P. Bernardini, S. Menchetti, A model for the mechanism of incorporation of cu, fe and zn in the stannite - kesterite series, Cu2FeSnS4 - Cu2ZnSnS4, Can. Mineral. 41 (2003) 639–647, https://doi.org/10.2113/gscanmin.41.3.639.

[27] S. Schorr, H.-J. Hoebler, M. Tovar, A neutron diffraction study of the stannite-kesterite solid solution series, Eur. J. Mineral 19 (2007) 65–73, https://doi.org/10.1127/0935-1221/2007/0019-0065.

[28] T. Shibuya, Y. Goto, Y. Kamihara, M. Matoba, K. Yasuoka, L.A. Burton, A. Walsh, From kesterite to stannite photovoltaics: stability and band gaps of the Cu 2 (Zn,Fe) SnS 4 alloy, Appl. Phys. Lett. 104 (2014), 021912, https://doi.org/10.1063/1.4862030.

[29] V.S. Vinila, R. Jacob, A. Mony, H.G. Nair, S. Issac, S. Rajan, A.S. Nair, J. Isac, XRD studies on nano crystalline ceramic superconductor Pb8rCaCuO at different treating temperatures, Cryst. Struct. Theor. Appl. (2014) 1–9, https://doi.org/10.4236/csta.2014.31001, 03.

[30] JCPDS card number 00-026-0575.

[31] X. Fontané, V. Izquierdo-Roca, E. Saucedo, S. Schorr, V.O. Yukhymchuk, M. Y. Valakh, A. Pérez-Rodríguez, J.R. Morante, Vibrational properties of stannite and kesterite type compounds: Raman scattering analysis of Cu2(Fe,Zn)SnS4, J. Alloys Compd. 539 (2012) 190–194, https://doi.org/10.1016/j.jallcom.2012.06.042.

[32] P.A. Fernandes, P.M.P. Salomé, A.F. da Cunha, Growth and Raman scattering characterization of Cu2ZnSnS4 thin films, Thin Solid Films 517 (2009) 2519–2523, https://doi.org/10.1016/j.tsf.2008.11.031.

[33] B.K. Sarkar, A.S. Verma, P.S. Deviprasad, Temperature induced band gap shrinkage in Cu2GeSe3: role of electron–phonon interaction, Phys. B Condens. Matter 406 (2011) 2847–2850, https://doi.org/10.1016/j.physb.2011.04.045.

[34] M. Dimitrievska, A. Fairbrother, X. Fontané, T. Jawhari, V. Izquierdo-Roca, E. Saucedo, A. Pérez-Rodríguez, Multiwavelength excitation Raman scattering study of polycrystalline kesterite Cu 2 ZnSnS 4 thin films, Appl. Phys. Lett. 104 (2014), 021901, https://doi.org/10.1063/1.4861593.

[35] A. Khare, B. Himmetoglu, M. Johnson, D.J. Norris, M. Cococcioni, E.S. Aydil, Calculation of the lattice dynamics and Raman spectra of copper zinc tin chalcogenides and comparison to experiments, J. Appl. Phys. 111 (2012), 083707, https://doi.org/10.1063/1.4704191.

[36] L.S. Price, I.P. Parkin, A.M.E. Hardy, R.J.H. Clark, T.G. Hibbert, K.C. Molloy, Atmospheric pressure chemical vapor deposition of tin sulfides (SnS, Sn 2 S 3 , and SnS 2) on glass, Chem. Mater. 11 (1999) 1792–1799, https://doi.org/10.1021/cm990005z.

[37] M. Steichen, R. Djemour, L. Gütay, J. Guillot, S. Siebentritt, P.J. Dale, Direct synthesis of single-phase p-type SnS by electrodeposition from a dicyanamide ionic liquid at high temperature for thin film solar cells, J. Phys. Chem. C 117 (2013) 4383–4393, https://doi.org/10.1021/jp311552g.

[38] S. Khalid, M.A. Malik, D.J. Lewis, P. Kevin, E. Ahmed, Y. Khan, P. O'Brien, Transition metal doped pyrite (FeS 2) thin films: structural properties and evaluation of optical band gap energies, J. Mater. Chem. C 3 (2015) 12068–12076, https://doi.org/10.1039/C5TC03275J.

[39] M. Himmrich, H. Haeuseler, Far infrared studies on stannite and wurtzstannite type compounds, Spectrochim. Acta Part A Mol. Spectrosc. 47 (1991) 933–942, https://doi.org/10.1016/0584-8539(91)80283-O.

[40] P.A. Fernandes, P.M.P. Salomé, A.F. da Cunha, A study of ternary Cu 2 SnS 3 and Cu 3 SnS 4 thin films prepared by sulfurizing stacked metal precursors, J. Phys. D Appl. Phys. 43 (2010), 215403, https://doi.org/10.1088/0022-3727/43/21/215403.

[41] M. Sebai, I. Trabelsi, M. Kanzari, Comparative study of electrical properties of Cu2ZnxFe1 –xSnS4 thin films, Mater. Sci. Eng., B 240 (2019) 55–61, https://doi.org/10.1016/j.mseb.2019.01.004.

[42] M.H. Ehsani, P. Kameli, M.E. Ghazi, Influence of grain size on the electrical properties of the double-layered LaSr 2Mn 2O 7 manganite, J. Phys. Chem. Solid. 73 (2012) 744–750, https://doi.org/10.1016/j.jpcs.2012.01.020.

[43] K.C. Wang, P. Chen, C.M. Tseng, Facile one-pot synthesis of Cu2ZnSnS4 quaternary nanoparticles using a microwave-assisted method, CrystEngComm 15 (2013) 9863–9868, https://doi.org/10.1039/c3ce41691g.

[44] R. Aruna-Devi, M. Latha, S. Velumani, J. Santos-Cruz, R. Murali, J.-Á. Chávez-Carvayar, F.A. Pulgarín-Agudelo, O. Vigil-Galán, Cu 2 ZnSn(S,Se) 4 thin-films prepared from selenized nanocrystals ink, RSC Adv. 9 (2019) 18420–18428, https://doi.org/10.1039/C9RA02669J.

[45] S.W. Shin, S.M. Pawar, C.Y. Park, J.H. Yun, J.-H. Moon, J.H. Kim, J.Y. Lee, Studies on Cu2ZnSnS4 (CZTS) absorber layer using different stacking orders in precursor

thin films, Sol. Energy Mater. Sol. Cells 95 (2011) 3202–3206, https://doi.org/10.1016/j.solmat.2011.07.005.
[46] H. Liu, Universal dielectric relaxation induced giant dielectric permittivity in Mn-doped PbZrO 3 ceramics, Ceram. Int. 45 (2019) 10380–10384, https://doi.org/10.1016/j.ceramint.2019.02.096.
[47] H. Liu, Y. Sun, Defect chemistry for Mn-doped and Nb-doped BiFeO3-based ceramics, J. Phys. Chem. Solid. 170 (2022), 110951, https://doi.org/10.1016/j.jpcs.2022.110951.
[48] A. Tang, Z. Li, F. Wang, M. Dou, Y. Pan, J. Guan, One step electrodeposition of Cu2ZnSnS4 thin films in a novel bath with sulfurization free annealing, Appl. Surf. Sci. 402 (2017) 70–77, https://doi.org/10.1016/j.apsusc.2017.01.079.
[49] C. Loha, R. Das, B. Choudhury, Evaluation of air drying characteristics of sliced ginger (zingiber officinale) in a forced convective cabinet dryer and thermal conductivity measurement, J. Food Process. Technol. (2012), https://doi.org/10.4172/2157-7110.1000160, 03.
[50] A.K. Jonscher, Nature 267 (1977) 673.
[51] U. Megha, G. Varghese, K. Shijina, Room temperature ac impedance and dielectric studies of Bi and Sr doped PrCo0.6Fe0.4O3 perovskites, Process, Appl. Ceram. 11 (2017) 52–59, https://doi.org/10.2298/PAC1701052M.
[52] N.F. Mott, E.A. Davis, in: Electronic Processes in Non-crystalline Materials by N. F. MOaT and E. A. DAVIS, Clarendon Press: Oxford Univ. Press, Oxford, 1971, p. 437.
[53] I. Trabelsi, A. Harizi, M. Kanzari, Complex impedance spectroscopy of Sn 4 Sb 6 S 13 thin films deposited by thermal vacuum evaporation, Thin Solid Films 631 (2017) 161–171, https://doi.org/10.1016/j.tsf.2017.04.028.
[54] R. Dridi, I. Saafi, A. Mhamdi, A. Matri, A. Yumak, M. Haj Lakhdar, A. Amlouk, K. Boubaker, M. Amlouk, Structural, optical and AC conductivity studies on alloy ZnO–Zn2SnO4 (ZnO–ZTO) thin films, J. Alloys Compd. 634 (2015) 179–186, https://doi.org/10.1016/j.jallcom.2015.02.009.
[55] V. Biju, M.A. Khadar, Dielectric properties of nanostructured nickel oxide, J. Mater. Sci. 38 (2003) 4055–4063, https://doi.org/10.1023/A:1026131103898.
[56] S. Kurien, J. Mathew, S. Sebastian, S.N. Potty, K.C. George, Dielectric behavior and ac electrical conductivity of nanocrystalline nickel aluminate, Mater. Chem. Phys. 98 (2006) 470–476, https://doi.org/10.1016/j.matchemphys.2005.08.080.
[57] A. Mhamdi, B. Ouni, A. Amlouk, K. Boubaker, M. Amlouk, Study of nickel doping effects on structural, electrical and optical properties of sprayed ZnO semiconductor layers, J. Alloys Compd. 582 (2014) 810–822, https://doi.org/10.1016/j.jallcom.2013.08.080.
[58] R. Ondo-Ndong, G. Ferblantier, F. Pascal-Delannoy, A. Boyer, A. Foucaran, Electrical properties of zinc oxide sputtered thin films, Microelectron. J. 34 (2003) 1087–1092, https://doi.org/10.1016/S0026-2692(03)00198-8.
[59] S.S.N. Bharadwaja, P. Victor, P. Venkateswarulu, S.B. Krupanidhi, Ac transport studies of La-modified antiferroelectric lead zirconate thin films, Phys. Rev. B 65 (2002), 174106, https://doi.org/10.1103/PhysRevB.65.174106.
[60] P. Venkateswarlu, A. Laha, S.B. Krupanidhi, AC properties of laser ablated La-modified lead titanate thin films, Thin Solid Films 474 (2005) 1–9, https://doi.org/10.1016/j.tsf.2004.02.101.
[61] A.A. Ebnalwaled, Hopping conduction and dielectric properties of InSb bulk crystal, Int. J. Basic Appl. Sci. IJBAS-IJENS. 11 (2011).
[62] S.R. Elliott, A theory of a.c. conduction in chalcogenide glasses, Philos. Mag. A 36 (1977) 1291–1304, https://doi.org/10.1080/14786437708238517.